Tailoring wavelength and emitter-orientation dependent propagation of single photons in silicon nanowires

Mélodie Humbert, Peter Wiecha, Gérard Colas Des Francs, Xiao Yu, Nicolas Mallet, Aurélie Lecestre, Guilhem Larrieu, Vincent Larrey, Frank Fournel, Laurence Ressier, et al.

HAL Id: hal-03611963

https://hal.science/hal-03611963

Submitted on 17 Mar 2022

Tailoring wavelength and emitter-orientation dependent propagation of single photons in silicon nanowires

Mélodie Humbert,[1, 2] Peter R. Wiecha,[3] Gérard Colas des Francs,[4] Xiao Yu,[4] Nicolas Mallet,[3] Aurélie Lecestre,[3] Guilhem Larrieu,[3, 5] Frank Fournel,[6, 7] Vincent Larrey,[6, 7] Laurence Ressier,[2] Christian Girard,[1] Vincent Paillard,[1] and Aurélien Cuche[1]

[1]*CEMES, Université de Toulouse, CNRS (UPR 8011), Toulouse, France*
[2]*LPCNO, Université de Toulouse, CNRS, INSA, UPS, Toulouse, France*
[3]*LAAS, Université de Toulouse, CNRS, INP, Toulouse, France*
[4]*ICB, UMR 6303, Université de Bourgogne-Franche Comté, Dijon, France*
[5]*LIMMS-CNRS/IIS, Institute of Industrial Science, The University of Tokyo, Tokyo, Japan*
[6]*Université Grenoble Alpes, Grenoble, France*
[7]*CEA, LETI, MINATEC Campus, Grenoble, France*
(Dated: April 22, 2021)

Quantum nano-optics aims at transposing the concepts of quantum optics at the nanoscale. In this context, nitrogen-vacancy color centers in nanodiamonds are particularly interesting sources as they emit single photons one by one with a broad spectral distribution between 600 and 800 nm. We deposit such quantum emitters at the extremities of silicon nanowires and analyze the effects of this interaction via spectrally resolved confocal microscopy. We demonstrate that the single photon emission can be guided over several microns under conservation of their quantum statistics, and with efficiencies of up to 15 %.n We show that the silicon nanowires can be used as spectral filters for the quantum emission. Numerical simulations are in very good agreement with experiments, and indicate that the modal landscape of these nano-waveguides and the according coupling efficiencies with quantum emitters can be designed such that only light from emitters of specific orientations is efficiently guided through the nanowire, enabling a unique quantum state selectivity at a micrometer length scale. Our work opens the door to a genuine modal control of single photon transfer in sub-wavelength nanowaveguides, paving the way to future fundamental studies and towards integrated and multi-wavelength photonics applications in quantum nano-optics.

keywords: Quantum nano-optics, waveguide, nanowire, silicon, nitrogen-vacancy center

INTRODUCTION

Exploiting and controlling the quantum properties of light at short range is a crucial challenge for quantum technologies, and in particular for quantum communications. In the recent past huge effort has been put in the development of integrated photonic platforms for the miniaturization of quantum experiments with entangled photon pairs or indistinguishable photons [1, 2]. Nevertheless, until now typical integrated quantum photonics platforms still cover areas in the order of square millimeters. The development of actual nanoscale quantum devices remains an important open challenge [3, 4].

Designing the propagation of single quanta at a sub-wavelength scale is of major interest for integrated optical quantum information transfer. Controlling the single photon propagation is crucial for the design of optical communication channels between integrated qubits [5]. For this purpose, nanoscale single photon sources such as quantum dots, molecules or color-centers in nanocrystals have been positioned in the vicinity of photonic nanostructures, to enhance the emission rate, to control the radiation properties and to tailor the propagation of single photons. For instance, the interaction of quantum emitters with sub-wavelength plasmonic unidimensional nano-channels which support confined plasmonic modes has been recently studied [6–11]. Coupling to such localized modes can strongly modify the photodynamics of the emitters and effectively channel the excited plasmons. With such integrated quantum-plasmonics approaches the excitation of single quantized plasmons as well as single plasmon interferences have been demonstrated [12–14]. However, plasmonic nanostructures suffer from high ohmic losses, which is especially inconvenient for single photon applications with weak light flux. Hybrid solutions, combining plasmonics and dielectric waveguides have been proposed, in an attempt to minimize the ohmic losses by decreasing the footprint of the metallic part [11, 15–18].

Recently, high refractive index dielectric nanostructures have been considered as promising low-loss alternative to plasmonics [19]. Compared to metallic nanostructures, high-index dielectrics offer a sub-wavelength confinement of light along with tremendously lower dissipative losses [20]. Thus, all-dielectric nanostructures represent a promising platform to control the propagation of single photons via modal engineering at the nanoscale [19, 21, 22]. Another implicit advantage of certain high-index dielectrics such as silicon is their compatibility with CMOS fabrication technology. Yet, only recently broader research interest has begun to be explicitly dedicated to

all-dielectric quantum nano-photonics platforms.

Our work aims at developing a thorough understanding of the interaction between quantum emitters and all-dielectric nanowires. We study several aspects of the coupling of single photons to crystalline silicon nanowires (SiNWs) of varying size as well as their propagation properties. We use as nanometer-scale quantum light source, photostable color center hosted by nanodiamonds (NDs), which emit single photons in the visible spectrum with a broadband wavelength distribution. We position those NDs close to an extremity of SiNWs and experimentally analyze the consequences of this interaction on the emitter decay rate, and on the efficiency of the wavelength-dependent single photon transmission through the nanowaveguide as the width is changed. Subsequently, we study effects with respect to the wavelength and orientation of the emitting dipole transition. Our hyperspectral measurements and theoretical analysis suggests that the SiNW platform offers a rich modal landscape that can be extended to emitter-orientation selective quantum sorting, offering an exciting new degree of freedom for quantum applications in nano-optics.

RESULTS AND DISCUSSION

Experimental setup

We study the interaction of broadband quantum emitters with rectangular silicon nanowires (SiNWs) as illustrated in Fig. 1a. As broadband source of single photons we use negatively charged nitrogen-vacancy defects (NVs) in nanodiamonds (NDs) with a mean diameter of around 40 nm. A typical room-temperature emission spectrum of an isolated ND lying on the bare SiO_2 substrate is shown in Fig. 1c. We drop-cast a diluted dispersion of the NDs on a sample with a large number of identical SiNWs, and subsequently select the nanowires having a single ND located at one of their extremities. The SiNWs are fabricated on a transparent silicon-on-silica substrate (SOS) by ebeam lithography and subsequent reactive ion dry-etching (RIE) [23–25]. The length and height of the nanowires in our experiments are fixed to 7µm and 90 nm respectively. More details on the sample fabrication and preparation are given in the Methods section.

Figure 1a illustrates our experimental setup. The linear polarized light of a green laser ($\lambda_L = 532$ nm) is tightly focused by a ×100 high-NA objective onto a ND in order to excite the NVs. The laser can be operated either in continuous or pulsed mode. The polarization of the laser is constantly kept perpendicular to the long axis of the nanowires (see the supporting information). The sample lies on a xy piezo stage to allow nanometric spatial positioning. Through the same high-NA objective, we collect the light emitted by the NV centers, removing
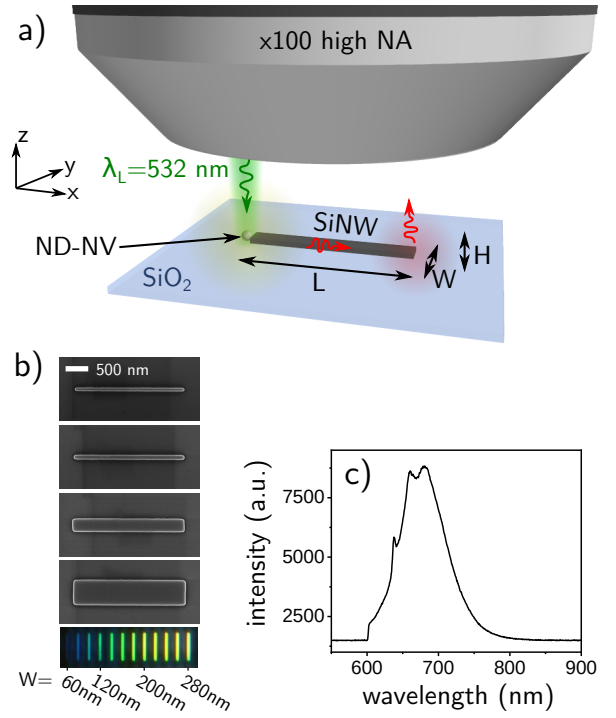

FIG. 1: (a) Illustration of the experimental configuration. A green laser is focused on a nano-diamond (ND, small sphere) containing few single photon emitters (NVs), coupled to one extremity of a rectangular-shaped SiNW, all lying on a transparent substrate (SiO_2). The green laser has a linear polarization perpendicular to the NW axis. The emission of the ND-NV is collected by the same high NA objective, reflected laser light is filtered by a dichroic mirror. Light guided to the opposite NW extremity is spatially selected by a pinhole in a conjugated image plane. (b) Selected SEM images of e-beam fabricated crystalline silicon nanowires with different widths (from top to bottom: W=30, 75, 200, 400 nm). Below, a dark-field microscopy image of several nanowires is shown with widths between 60 nm (left) and 280 nm (right). (c) Typical emission spectrum of the ND-NVs single photon emitters.

the laser with a dichroic mirror filter. In order to detect light emitted from a spatially narrow region (i.e. the opposite tip of the SiNW) we add a mobile 75 µm large pinhole in a conjugated image plane. The collected light is then analyzed either by a spectrometer, by an intensity correlator to obtain quantum statistics, or by lifetime measurements on the excited emitter. Alternatively we image the in-plane propagation of light by removing the pinhole and taking snapshots of the whole image plane with a highly sensitive EMCCD camera. More details on the experimental setup can be found in the Methods section.

Representative scanning electron microscopy (SEM) images of the studied nanowires are shown in figure 1b together with a dark-field microscopy image of a few SiNWs of increasing width (left to right: W=60 to 280 nm). The blue-to-yellow transition in the perceived color
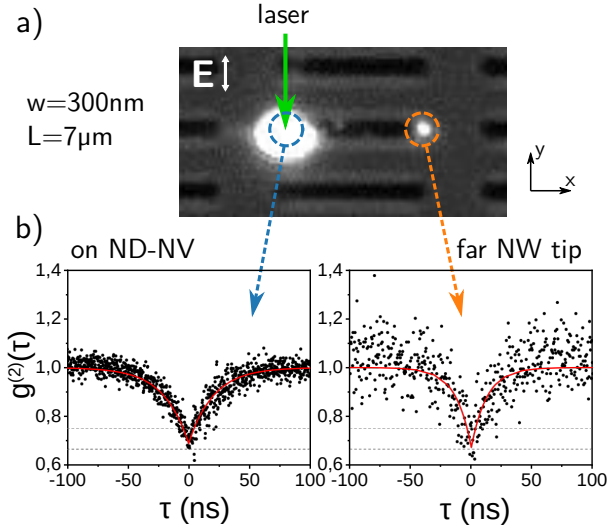
FIG. 2: (a) Bright-field microscopy image of the excited ND-NV at the tip of a SiNW. The laser light was removed by an optical low-pass filter. The laser polarization is indicated by a white arrow. (b) Second-order correlation functions of the emission from the ND-NV (illuminated by the laser as indicated by the green arrow in the top panel). The signal is acquired either directly on the ND (left) or from the opposite SiNW tip after propagation through the wire (right). The experimental data (black dots) are fitted with a two-level model for the autocorrelation function (red line). The fit indicates that 3 NV^- centers contribute to the signal. The bottom and top horizontal dotted lines indicate the range of $g^{(2)}(0)$ values corresponding to statistics for 3 individual single photon emitters.

is a consequence of red-shifted fundamental and high-order Mie-type resonances in the nanowires of increasing size. These resonances can be described by electric and magnetic multipole moments [26, 27] and are responsible for several phenomena such as significant near-field enhancement [28, 29] or strong directivity of scattered light [30, 31].

Number of single photon emitters (NV) per ND

To ensure that our experimental results stem exclusively from a true quantum emission, we first measure the second-order correlation function of the emission directly from the nanodiamond, as illustrated in figures 2a and b (left panel). We then place the pinhole in the image plane on the remote NW extremity to obtain statistics from the single photons that traveled through the SiNW. The corresponding second order correlation function fit (red curve - right plot in figure 2b) confirms that the quantum statistics are conserved through the nanowire. Both cases (measurement on the ND and on the opposite NW end) show a dip at zero delay with $0.66 < g^{(2)}(0) < 0.75$, confirming a sub-Poissonian emission statistics of the source.

These limits are indicated by the lower, respectively upper horizontal dashed lines in figure 2b. We can conclude that for the case shown in figure 2, three photons at maximum are guided simultaneously.

To exclude effects due to the specific orientation of the transition dipoles associated to each NV, we only select NV-SiNW systems which host a number between $3 < NV < 10$. In case a ND contains 3 or more independent emitters, these NVs can be approximated as scalar quantum emitters (see the supporting information) [32–34]. Having no experimental control on the NV emitter orientation, the simplification to a scalar quantum emitter is necessary in the following to allow a direct quantitative comparison of the different coupled ND-SiNW systems.

Spectral cut-off, single-photon wavelength filtering

Having confirmed that single-photon emission can be effectively guided by the SiNWs without losing its quantum character, we want to study the spectral consequences on the broadband quantum emission, since the NV^- centers in the nanodiamonds emit single photons at random wavelength ($600 \leq \lambda \leq 800$ nm – see spectrum in figure 1c). To numerically model our NV-SiNW system, we perform frequency domain simulations based on the Green's Dyadic Method (GDM). We consider that the emitting quantum system behaves like an electric dipole moment $\mathbf{p}$ placed at $\mathbf{r}'$, oscillating with frequency ω_0.

$$\mathbf{p}(t) = \mu_{12}\mathbf{u}\cos(\omega_0 t) \tag{1}$$

μ_{12} is the transition moment of the emitter, which is orientated along the unit vector $\mathbf{u}$. The emitted electromagnetic field can be obtained at any point $\mathbf{r}$ via the Green's tensor $\mathbf{G}$ that is associated with the complex environment [35]:

$$\mathbf{E}(\mathbf{r}, \omega_0) = \mathbf{G}(\mathbf{r}, \mathbf{r}', \omega_0) \cdot \mathbf{p}(\omega_0). \tag{2}$$

The Green's tensor for the environment containing the SiNW can be numerically calculated through a volume discretization of the nanowire in N mesh-cells and a subsequent inversion of the resulting discretized Dyson's equation [36]:

$$\mathbf{G}(\mathbf{r}, \mathbf{r}', \omega_0) = \mathbf{G}_{\mathrm{env}}(\mathbf{r}, \mathbf{r}', \omega_0) + \sum_{i=1}^{N} \mathbf{G}_{\mathrm{env}}(\mathbf{r}, \mathbf{r}_i, \omega_0) \frac{V_i \Delta\epsilon_i}{4\pi} \mathbf{G}(\mathbf{r}_i, \mathbf{r}', \omega_0) \tag{3}$$

where $\mathbf{G}_{\mathrm{env}}$ is the Green's tensor of the environment without nanowire (in our case describing the SiO_2 substrate of refractive index $n_{\mathrm{sub}} = 1.45$), V_i is the volume of the ith mesh cell situated at $\mathbf{r}_i$ with a permittivity
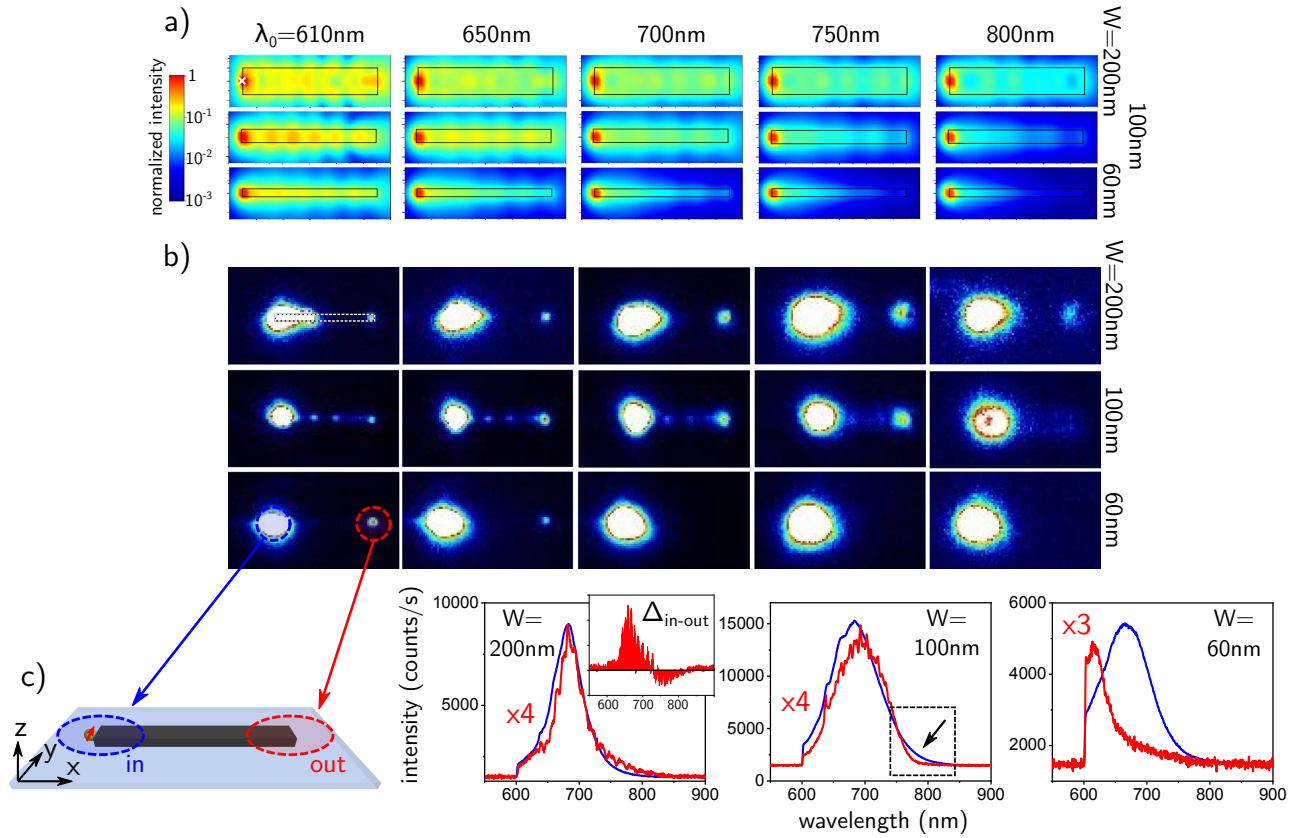
FIG. 3: (a) Simulated intensity of the electric field 30 nm above 1 μm long nanowires for five different emitter-wavelengths (from left to right: λ= 610, 650, 700, 750 and 800 nm) and for three typical nanowire widths (from top to bottom: 200, 100 and 60 nm). The position of the dipolar emitter is indicated by a white cross in the top left image. Each map shows the incoherent average of three dipole orientations (along x, y and z). (b) Series of wide-field luminescence images acquired using five different narrow-band bandpass filters centered around $λ_{BP}$= 610, 650, 700, 750 and 800 nm (from left to right). The shown nanowires have a length of 7 μm and widths of 200, 100 and 60 nm (top to bottom). The outline of the SiNW is indicated in the top left panel by a dashed rectangle. (c) NV emission spectra recorded at the two extremities of the SiNWs (as indicated in the sketch on the left by blue and red circles). From left to right the width of the nanowire is 200, 100 and 60 nm. The measurement on the ND is plotted as blue lines, the spectra acquired on the opposite extremity is shown in red and multiplied by a factor between 3 and 4 for better comparability (as indicated). For $W = 200$ nm, the difference between the input and the output spectrum (after normalization) is shown in the inset. In the case of the $W = 100$ nm SiNW, the cut-off spectral region around 800 nm is indicated by a dashed square inset and a small arrow, to highlight the suppression of the transmission.

contrast relative to the background medium of $Δ\epsilon_i$. For details see e.g. Ref. [35]. We perform our simulations using our homebuilt 3D-GDM toolkit "pyGDM" [37].

In figure 3a we show systematic GDM simulations, where we use equation (2) to calculate the electric field at a height of 30 nm above 1 μm long and 90 nm high SiNWs of variable width (200 nm, 100 nm and 60 nm, top to bottom panels). An oscillating dipole is positioned at the center of the SiNW's left edge (indicated by the white cross in the top left panel). This dipole transition is emitting at wavelengths $λ_0$ between 610 nm and 800 nm (panels from left to right). According to the scalar emitter assumption for our experimental emitters, we show here the incoherent sum of the electric field intensity maps for three perpendicular dipole orientations (see the supporting information). The permittivity of silicon is taken

from literature [38]. In addition, the simulations account for the silica substrate. Figure 3b shows the results of hyperspectral measurements, with a set of image planes of the ND-SiNW system for different NW widths, filtered by narrow bandpass filters at the same wavelengths as the simulations. The filters have a spectral width of $Δλ = 10$ nm. Each image plane map is normalized to the peak intensity (hence to the intensity at the ND-NV location) and the colorscale is clipped in order to improve the visibility of the remote end luminescence for this qualitative comparison. The transmitted intensity is usually in the order of around 2 % up to 15 % of the emitted intensity measured directly on the ND-NV, which will be discussed in more detail below.

Spectra corresponding to the emission in figure 3b are shown in figure 3c. The emission was collected either on

the ND-NV ("in", blue lines) or from the remote end of the nanowire ("out", red lines). We note that the SiNW acts as a (low Finesse) Fabry-Perot cavity, which can be seen by some regular oscillations on the spectra measured after transmission through the SiNWs (see e.g. red line spectrum in Fig. 3c, $W = 200\,\text{nm}$). The fringe visibility is modest because of the rugosity and defects of the SiNW side-walls, as a results of the RIE fabrication step.

In agreement with the numerical near-field simulations, we find that the largest nanowires, guide the whole spectrum of the broadband single-photon emission towards their remote extremity (see case $W = 200\,\text{nm}$). For SiNWs of a width of $W = 100\,\text{nm}$, we observe a diminution of the transmission at the long wavelength end of the spectrum (c.f. case $\lambda_0 = 800\,\text{nm}$ in figure 2b; see also dashed box and arrow in the $W = 100\,\text{nm}$ sub-figure of 3c). Decreasing further the nanowire width down to $W = 60\,\text{nm}$ leads to an extinction of the transmitted light for wavelengths $\lambda_0 \gtrsim 650\,\text{nm}$. As will be discussed in detail below, this cut-off be explained by the disappearance of any guided modes below a certain size of the nanowire. In conclusion, we demonstrate in figure 3, that the broad-band single-photon emission from NVs in nanodiamonds can be spectrally filtered at a micrometer length scale via silicon nanowires.

Supported guided modes and related propagation lengths

In the following we want to understand the mechanisms behind the observed spectral cut-off. To this end, we regard the rectangular shaped SiNWs as classical waveguides.

To determine the guided modes of the SiNWs, we use an approach based on the photonic local density of states (LDOS). According to Fermi's golden rule, the LDOS is proportional to the decay rate of a quantum emitter. It hence quantifies the number of locally available decay channels for a transition dipole. The *partial* LDOS describes the available decay channels for an emitter of specific orientation $\alpha \in \{x, y, z\}$. It is proportional to the imaginary part of the diagonal elements of the Green's tensor Eq. (3) and writes [39]:

$$\rho_\alpha(\mathbf{r}, \omega_0) = \frac{1}{2\pi^2\omega_0}\text{Im}\Big(\mathbf{G}_{\alpha\alpha}(\mathbf{r}, \mathbf{r}, \omega_0)\Big). \quad (4)$$

To make the link to the guided modes contributing to the LDOS, we use a Weyl expansion of the LDOS for a structure with an infinitely long axis (the SiNW axis along x in our coordinate system) and define a 2D-LDOS [40, 41]:

$$\rho_\alpha^{2D}(\mathbf{r}, k_x, \omega_0) = \frac{1}{2\pi^2\omega_0}\text{Im}\Big(\mathbf{G}_{\alpha\alpha}^{2D}(\mathbf{r}_\parallel, \mathbf{r}_\parallel, k_x, \omega_0)\Big). \quad (5)$$

In the latter case, $\mathbf{r}_\parallel$ is a location in the yz plane and ρ_α^{2D} is proportional to the decay rate of an *infinitely long*

line of dipole emitters of orientation α, parallel to the NW axis. The 2D and 3D Green's tensors are linked by a Fourier transform [42]. This Weyl expansion of the 3D density of states via the 2D-LDOS shows Lorentzian resonance profiles as function of k_x (see also the supporting information). Its complex effective index $\widetilde{n_{\text{eff}}} = n'_{\text{eff}} + \text{i}n''_{\text{eff}}$ can be numerically extracted by fitting the resonance of the Weyl expansion with a Lorentzian [41]. If the effective index $k_x/k_0 = n_{\text{eff}}$ of such a resonance is greater than the substrate index n_{sub}, it is associated to a propagating guided mode. This technique allows also to calculate the propagation length of a mode via the imaginary part of $\widetilde{n_{\text{eff}}}$ as $L_{\text{prop}} = \lambda/(4\pi n''_{\text{eff}})$.

Figure 4a shows the guided modes existing in a SiNW of fixed height ($H = 90\,\text{nm}$) and variable width for vacuum wavelengths λ_0 of (i) 600 nm, (ii) 700 nm, and (iii) 800 nm. Red lines indicate transverse electric (TE) modes for which the electric field is parallel to the substrate plane. Blue lines correspond to transverse magnetic (TM) modes (electric field perpendicular to the substrate). As mentioned above, an effective index $n'_{\text{eff}} \gtrsim n_{\text{sub}}$ indicates a bound mode, whereas $n'_{\text{eff}} \lesssim n_{\text{sub}}$ is associated to a leaky mode, for which light can effectively leak into the substrate.

As can be seen in figure 4a, increasing the nanowire width naturally leads to an increasing number of supported waveguide modes. The same effect occurs for decreasing vacuum wavelengths. We also find that higher order TM modes occur significantly later than higher order TE modes. The fact that the last guided modes supported by the SiNW sequentially vanish for widths $W \lesssim 100\,\text{nm}$ explains the wavelength cut-off which we observe in figure 3 for small nanowires. For wavelengths $\lambda_0 \gtrsim 700\,\text{nm}$, we observe also that the transmission for the smallest nanowires is dominated by a single mode (TE_{00}).

Having identified the guided modes of the SiNWs, we can compare their propagation lengths (figure 4c) to the experimentally observed transmission efficiency Q_T (figure 4b). The transmission efficiency is the ratio of the maximum intensity measured at the remote end and the maximum intensity of the emission measured at the location of the ND-NV. Q_T is typically in the order of a few % for short wavelengths but can reach values up to 15% for longer wavelengths. This trend is in agreement with the average asymptotic propagation length of the supported guided modes (figure 4c), which increases with the wavelength from around 4 µm at $\lambda_0 = 600\,\text{nm}$, over 7 µm at $\lambda_0 = 700\,\text{nm}$ to around 11 µm for $\lambda_0 = 800\,\text{nm}$. The effect has also an influence on the transmitted spectra. In the inset of the subplot $W = 200\,\text{nm}$ in figure 3c, the subtraction of the normalized spectra taken directly on the ND-NV and on the remote end of the SiNW is plotted. The resulting difference shows that the signal transmitted by the NW is spectrally reshaped in favor of the long wavelength tail of the spectrum (with a normal-
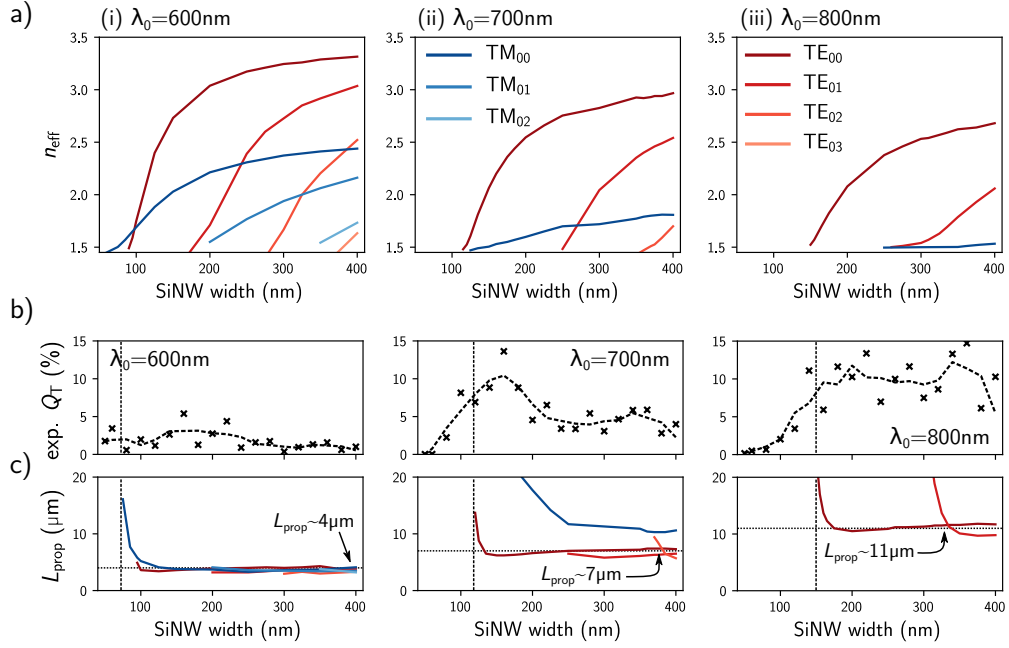
FIG. 4: (a) Effective index dispersion of the waveguide modes in rectangular wires as a function of the width W at a wavelength of (i) $\lambda_0 = 600\,\text{nm}$, (ii) $\lambda_0 = 700\,\text{nm}$ and (iii) $\lambda_0 = 800\,\text{nm}$. Calculated using 2D-GDM simulations, assuming an infinitely long nanowire. (b) Experimental transmission efficiency as function of the SiNW width for, from left to right, $\lambda_0 = 600\,\text{nm}$, $\lambda_0 = 700\,\text{nm}$ and $\lambda_0 = 800\,\text{nm}$. The dashed black line corresponds to the moving average over three neighbor points. (c) 2D-GDM simulated propagation length of each mode at wavelength $\lambda_0 = 600\,\text{nm}$, $\lambda_0 = 700\,\text{nm}$ and $\lambda_0 = 800\,\text{nm}$ (from left to right). Vertical dashed lines in (b-c) mark the onset of guided modes in the simulations.

ized difference of up to 25 % after normalization of both spectra). This is a consequence of the reduced propagation length at short wavelengths.

Interestingly, in the case of $\lambda_0 = 700\,\text{nm}$ we observe a region of particularly high transmission efficiency for nanowire widths around $W \approx 150\,\text{nm}$ (figure 4b). For our SiNWs on SiO_2, there is an increase of the propagation length near the cutoff $n_\text{eff} \approx n_\text{sub}$ which separates a regime of efficient propagation of light in the waveguide from a regime where leakage into the environment dominates (figure 4c). We therefore ascribe this increase of Q_T to the high propagation length of the TM_{00} mode in the regime where its effective index approaches the substrate refractive index. This effect, occurring at $\lambda_0 = 800\,\text{nm}$ too with the TE_{00} and TE_{01} modes, might explain the variations in intensity observed as a function of W. We want to emphasize here that the propagation lengths in silicon nanowires significantly surpass the propagation lengths of plasmonic single photon waveguides [11, 34].

Coupling efficiency to specific modes

After having demonstrated that the wavelength-dependent single-photon transmission is dictated by the properties of the guided modes of the SiNWs, we will now analyze the efficiency of the interaction as well as

which of the modes are preferentially populated by the photons. Subsequently we will discuss how this can be used to control the quantum emission beyond the above demonstrated wavelength filtering.

The coupling efficiency to a specific mode is defined as the ratio of the decay rate into this mode over the total decay rate, which is equivalent to the ratio of the respective LDOS [43]:

$$\beta_\text{mode} = \frac{\rho_\text{mode}}{\rho_\text{tot}} = \frac{\Gamma_\text{mode}}{\Gamma_\text{tot}}. \qquad (6)$$

The LDOS is proportional to the decay rate of an emitter, measuring its lifetime is therefore an appropriate experimental tool to probe variations of the LDOS. Figure 5a shows lifetime measurements and according simulations, either for the isolated ND (used as reference), or coupled to the extremity of a SiNW. The lifetimes are spectrally averaged over the entire emission spectrum and of course comprise all emitters in the nanodiamond. Each point is obtained from measurements of 5 independent NDs, the error bars correspond to one standard deviation. In the SI we show the experimental decay curves and the respective fits for all measured emitters. The lifetime measurements can be fitted well with a double exponential model, revealing a short (τ_1) and a long-living (τ_2) component in the luminescence. Those contributions are usually ascribed to surface effects (fast decay) and nitrogen vacancies (slow decay) [44]. We show both values
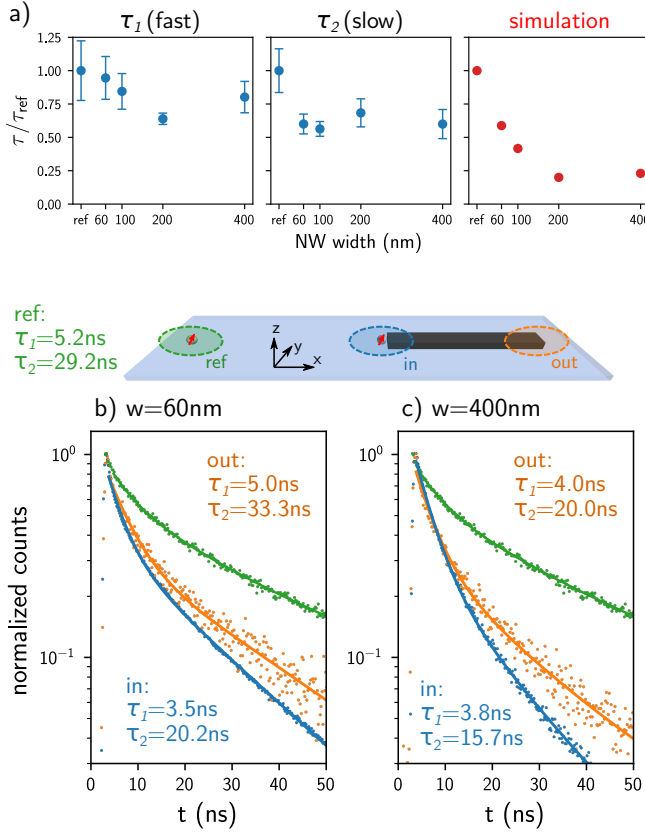
FIG. 5: (a) Lifetime measurements for ND-NVs coupled to the extremity of a SiNW as function of the nanowire width, normalized to an isolated emitter ("ref"). The slow and fast decay components are shown in the left, respectively center panels. The right panel shows the simulated lifetime reduction for an orientation-averaged dipole emitter at $\lambda_0 = 700$ nm. (b) Decay rates of a ND-NV coupled to a SiNW of width $W = 60$ nm. The reference decay rate (green) was measured on an isolated nanodiamond, lying on the bare substrate. (c) Same as (b) for a SiNW of $W = 400$ nm. Dots are experimental results, solid lines correspond to a double-exponential fit with a fast (τ_1) and a slow (τ_2) component. The sketch above (b-c) depicts the locations of the ND-NV and of the decay rate measurement. The detection is either on the ND-NV coupled to the NW (blue) or on the remote NW tip (orange), or on an isolated emitter lying on the bare substrate (green).

in figure 5, but want to emphasize that we are mainly interested in the long-living component τ_2. In the presence of the nanowire, an ≈ 2 fold enhancement of the long living lifetime τ_2 can be observed (blue dots), which is in reasonable agreement with our numerical 3D lifetime simulations (red dots, see also the supporting information). The simulated values correspond to the maximum LDOS enhancement at the NW extremity and are calculated at $\lambda_0 = 700$ nm (the peak of the emission wavelength). The variable positions of the NDs with respect to the extremity of the NWs in our samples may be a reason why the decay enhancement is overestimated by our simulations.

In figure 5b-c explicit lifetime measurements are shown for selected nanowires of widths of $W = 60$ nm, respectively $W = 400$ nm. Measurements were carried out either by collecting on the ND-NV (blue dots and lines), or after transmission through the SiNW at the opposite extremity (orange dots and lines). An isolated emitter is shown for comparison (green dots and lines). While we would intuitively expect the same lifetimes at the nanowire input and output, we consistently find around $30 - 50\%$ longer lifetimes τ_2 for the photons that pass through the SiNWs. In order to assess the origin of the observed differences, we first define the intensity measured directly on the ND $I_{\mathrm{ND}}(t) = I_0 e^{-\Gamma_{\mathrm{tot}} t}$ and the intensity at the NW output I_{out}, which, in case of a single mode waveguide, writes $I_{\mathrm{out}}(t) = \beta I_0 e^{-\Gamma_{\mathrm{tot}} t} e^{-L/L_{\mathrm{prop}}}$. $\Gamma_{\mathrm{tot}} = \Gamma_r + \Gamma_{\mathrm{wg}}$ is the total decay rate, including radiative rate (Γ_r) and coupling to the waveguide (Γ_{wg}, which does not depend on the propagation losses in the waveguide [43]). In this simplified model we neglect other non-radiative channels.

As stated above, in the case of a single quantum emitter, the lifetime should be the same whether measured directly on the emitter or after propagation through the waveguide. In our case however, the measured lifetime is an average over several emitters inside the nanodiamond. The decay rate and coupling efficiency of each emitter depends on its orientation, its position, on the emission wavelength as well as on the accessible guided modes. To disentangle the distinct modes, we would at least need to measure spectrally resolved lifetimes using bandpass filters. Unfortunately the low single photon flux leads to very long integration times, which practically renders such experiments out of reach with our experimental setup. Hence we can merely estimate the averaged coupling efficiency to all guided modes, averaged furthermore over the full emission spectrum. We assume that Γ_r is identical all the emitters within a single ND. Then we can express the emitter dynamics as function of β using $\Gamma_{\mathrm{tot}} = \Gamma_r + \beta \Gamma_{\mathrm{tot}} = \Gamma_r/(1 - \beta)$. The total signal from a nanodiamond can be calculated by a sum over the separate emitters (see supporting information). For a qualitative understanding of the dynamics, we convert the sum over all emitters to an integral over β, which apparently is a quite rough approximation in case of only few emitters. We obtain for the signal on the ND-NV (see supporting information for details on the derivation):

$$I_{\mathrm{ND}}(t) = \int_0^{\beta_{\mathrm{max}}} I_0 e^{-\Gamma_r t/(1-\beta)} d\beta \qquad (7)$$

where β_{max} is the highest existing coupling factor. Similarly, for the intensity measured at the waveguide output, we can derive (see also supporting information)

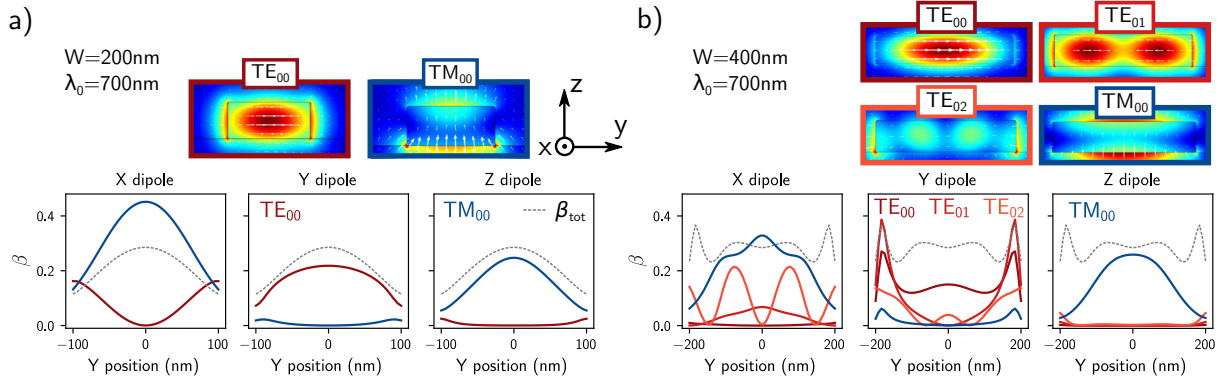$$I_{\mathrm{out}}(t) = \int_0^{\beta_c} \beta e^{-\Gamma_r t/(1-\beta)} d\beta \qquad (8)$$

FIG. 6: (a) Top: intensity profile sections of the supported guided modes of a $W = 200\,\text{nm}$ large SiNW at $\lambda_0 = 700\,\text{nm}$. Bottom: 2D simulations of the lateral profiles of the coupling efficiency to the available guided modes, calculated $Z = 10\,\text{nm}$ above an infinitely long SiNW for dipole orientations X (along NW axis), Y (along NW width) and Z (along NW height). (b) Same as (a) but for a NW width of $W = 400\,\text{nm}$.

Due to the limited propagation length, part of the dynamics will be lost at the waveguide extremity. Thus, β_c corresponds to a cut-off applied to β to remove the part of the signal that is significantly decreased. This cut-off is applied on the upper limit since low β contribute only weakly to the output signal.

These two expressions can qualitatively reproduce the measured dynamics for the $W = 60\,\text{nm}$ and $W = 400\,\text{nm}$ nanowires shown in figures 5b and 5c where we observed a shorter lifetime at the output. The best agreement is obtained with cut-off limits $\beta_c^{60} = 0.15$ and $\beta_c^{400} = 0.30$, respectively (see the supporting information). Although this simplified model represents only a rough estimation of the coupling factor, this approach provides a plausible explanation for the decreased decay rate observed at the NW remote extremity, which is a result of the incoherent sum of contributions of multiple emitters.

In order to affirm our estimation of β by the above decay rate analysis, we use an approach described in literature [18], using a launching point on the nanowire center and comparing the intensity of the ND-NV placed on the NW center relative to the intensities of guided light arriving at both NW extremities. For this analysis we picked SiNWs from our sample on which a ND-NV is attached close to the nanowire center (see SI Fig. S10). The two extremities shall be labelled A and B, the coupling efficiency in this system writes $\beta \simeq (I_A + I_B)/(I_A + I_B + I_{\text{ND}})$. We extracted the intensities scattered at these three positions from wide-field luminescence images of NDs positioned at an equidistant position from the two extremities A and B of $7\,\mu\text{m}$ long NWs with different widths $W = 60\,\text{nm}$ and $W = 400\,\text{nm}$ (see SI Fig. S10). For comparison with the lifetime measurements, we use images which are spectrally integrated over the entire NV emission. We also neglect again all non-radiative decay channels. The spectrally averaged transfer efficiencies are estimated from this acquisition in the same way as was

done for figure 4b. For both extremities (A and B) we obtain $\overline{Q_T^{60}} = 0.033$ and $\overline{Q_T^{400}} = 0.085$. The averaged propagation lengths are taken from 2D simulations, employing a spectral weighting using experimental emission spectra. We find $\overline{L_{\text{prop}}^{60}} = 6.89\,\mu\text{m}$ and $\overline{L_{\text{prop}}^{400}} = 6.94\,\mu\text{m}$, which leads to average coupling factors of $\beta^{60} = 0.1$ and $\beta^{400} = 0.22$. Those values are in good agreement with our estimations by decay rate analysis.

Since the experiment allows only to estimate an average coupling efficiency, we use numerical simulations to study the coupling to the individual modes in more detail. The aforementioned Weyl expansion of the LDOS (equation 5) can be used to identify all decay channels and their relative contributions to the total LDOS, it allows us calculating the coupling efficiency of an emitter to the individual guided modes at a given wavelength [40]. We note that the coupling efficiencies are based on 2D calculations, and therefore comprise forward and backward propagation.

Figure 6 shows the lateral profiles of the coupling efficiency β to the available modes for three perpendicular dipole orientations at the examples of SiNWs of width $W = 200\,\text{nm}$ (6a) and $W = 400\,\text{nm}$ (6b). The coupling efficiency profiles are calculated for emitters at a distance of $10\,\text{nm}$ above the SiNWs, radiating at $\lambda_0 = 700\,\text{nm}$. In case of the $W = 200\,\text{nm}$ nanowire, for x and z oriented dipoles we find a particularly high coupling efficiency to the TM_{00} mode, going up to almost $50\,\%$ for the x-dipole. Only a y-oriented emitter couples preferentially to the TE_{00} mode, but the total coupling efficiency (represented by a black dashed line) is dominated by the TM mode. This finding supports our hypothesis that the particularly high transmission efficiency, which we observed in figure 4b (center plot) for $\lambda_0 = 700\,\text{nm}$ and $W \leq 200\,\text{nm}$, is due to the increased propagation length of the TM_{00} mode. At the same emission wavelength but for a nanowire

width of $W = 400\,\text{nm}$, the coupling of x-dipoles to the fundamental TM mode is somewhat less efficient in favor of coupling to higher order TE modes. On the other hand, y dipoles still couple mainly to TE modes and z-oriented emitters populate exclusively the TM mode, in good agreement with the intensity maps and electric field lines in the yz plane presented in figure 6b.

The 2D simulations in figure 6 allow to analyze the available waveguide modes and their coupling efficiencies via the LDOS, and are helpful for a qualitative interpretation of the experiments. To go a step further and correctly account for the position of the ND-NV at the end facet of a nanowire, along with the three-dimensional nature and finite length of our SiNWs, we perform additional 3D-GDM simulations. We employ a complementary and more direct approach not based on the LDOS computation to identify the populated modes. We consider the SiNW as Fabry-Perot cavity of which we probe the transmitted field intensity (averaged over the whole NW facet cross section) upon coupling a dipole emitter $\mathbf{p}$ to the opposite end. We then gradually increase the length of the SiNW, as illustrated in figure 7a. Via a Fourier analysis of the transmitted intensity as function of the nanowire length L_{NM}, we can deduce the effective index of the guided modes which resonate in the nanowire cavity, since the free spectral range is proportional to the mode's effective wavelength $\lambda_{\text{eff}} = \lambda_0/n_{\text{eff}}$ in the cavity (see Fig. 7b-c).

In figure 7d-e we show the effective index of the populated waveguide modes for three perpendicular dipole orientations (x: green, y: red, z: blue) and for three different emission wavelengths (from left to right: 600 nm, 700 nm, and 800 nm). Figure 7d shows the case in which the dipole transition is centered in front of the SiNW facet. Fig. 7e shows the same simulations but with the quantum emitter displaced to the left by a quarter of the SiNW width.

In case of a quantum nanoemitter centered about the nanowire axis, we find that mostly one distinct guided mode contributes to the single photon transmission. x-dipoles couple preferentially to the TE_{01} mode, y-dipoles to the TE_{00} mode and z-dipoles to the TM_{00} mode. The weak coupling to the TM mode for both, x and y dipoles, can be explained with the emitter position in front of the SiNW. Because the TM_{00} mode profile has its maximum on top of the nanowire (see figure 6a), the according coupling efficiency is strongly reduced for emitter locations below the SiNW top surface. Hence the contribution of the TM mode to the guiding of the single photons vanishes. To test our assumption of height-dependent coupling to the fundamental TM mode, we performed the same 3D simulation as in figure 7d but with a dipole emitter on top of the SiNW end, which is shown in the supporting information. This modification of the ND-NV position results in a predominant coupling of z-dipoles to

the TM_{00} mode over large parts of the parameter space, in agreement with our 2D simulations. However, x-dipole coupling remains low in the 3D case.

The bottom subplots of figure 7d-e show the integrated transmission (all modes) as function of the NW width for the different dipole orientations. We observe that the y-dipole couples most efficiently to the TE_{00} mode. In a certain range of SiNW widths this is even the predominant transmission channel (e.g. around 200-250 nm for $\lambda_0 = 800\,\text{nm}$).

This yields to the conclusion that the strongly varying relative coupling to the different modes allows to use SiNWs to filter light from specific emitter-orientations. For instance at a wavelength of $\lambda_0 = 800\,\text{nm}$, a $W = 200\,\text{nm}$ SiNW preferentially transmits photons from y-oriented emitters. At a wavelength of $\lambda_0 = 600\,\text{nm}$ on the other hand, the same nanowire transmits mainly photons emitted by x-dipoles. As shown in the supporting information figure S8, placing the emitter on top of the SiNW offers a possible configuration to selectively filter z-oriented dipoles. This orientation-filtering phenomenon is strongly dependent on the relative position of the quantum source, as can be seen in Fig. 7e where the emitter is displaced off the SiNW axis. In this case the x and y oriented emitters typically couple to a mix of modes and the SiNWs cannot be used for orientation-selective filtering (see bottom row in Fig. 7e). Only z-dipoles still couple preferentially to a single mode (TM_{00}). For instance, narrow SINWs could be used to preferentially select photons emitted by z oriented emitters independently of the position of the ND at the NW edge. This behavior is also in agreement with our 2D simulations of the spatial distribution of the coupling efficiency on top of the SiNW waveguide (see figure 6a-b). It already shows that a genuine modal control of the transmission is possible with simple structures. It could be further improved through an accurate positioning of the quantum source with respect to the SiNW.

CONCLUSION

In conclusion, we have experimentally coupled nanodiamonds containing negatively charged nitrogen-vacancy centers to silicon nanowires of different sizes. Thanks to hyperspectral experiments, we demonstrated that the bandwidth of the broadband single-photon emission from the ND-NVs can be finely tuned using accordingly tailored SiNWs. The quantum character of the photons is conserved after transmission through the SiNWs, enabling a spatial control on the single photon emission. Via an original time-resolved approach and an extensive 2D and 3D numerical simulations we unveiled the role of guided modes in the photo-dynamics of the quantum emitters and studied the contributions of the nanowire modes to the photonic local density of states. We found
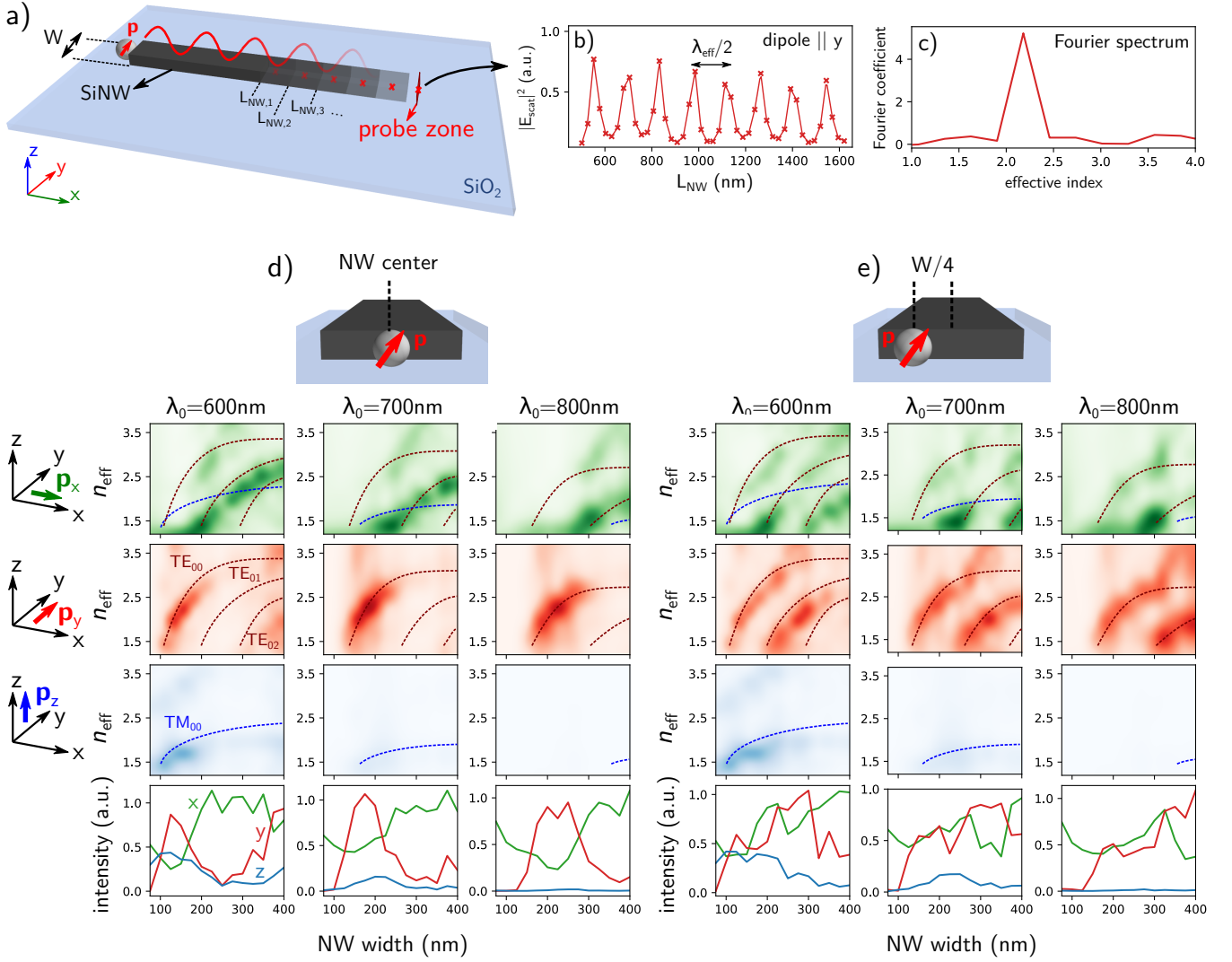
FIG. 7: Numerical 3D investigation of mode-specific coupling of the ND-NV (a) Sketch of the simulation principle: A series of simulations with increasing SiNW length is performed, calculating the electric field intensity of a quantum emitter (NV) transmitted through the SiNW. (b) The oscillation of the transmitted field intensity as function of SiNW length gives access to the effective wavelength inside the SiNW-cavity, the corresponding Fourier spectrum (c) reveals the respective contributions of the different modes by their effective index. (d) Fourier spectra at several emitter wavelengths for NW widths between $W = 50\,\mathrm{nm}$ and $W = 400\,\mathrm{nm}$ for the case in which the quantum emitter is placed centred in front of the SiNW. From top to bottom, the oscillating dipole is oriented along X, Y and Z, the emission wavelength is $\lambda_0 = 600\,\mathrm{nm}$, $\lambda_0 = 700\,\mathrm{nm}$ and $\lambda_0 = 800\,\mathrm{nm}$ (left to right). As a guide to the eye the guided modes which are mainly occupied are indicated by dashed lines (following the 2D simulations of figure 4). The bottom row shows the average transmitted intensity for each orientation as function of the nanowire width. (e) Same as (d) but with the quantum emitter displaced by $W/4$ towards the SiNW side border.

that depending on the emission wavelength, on the ND-NV position as well as on the orientation of the quantum emitter dipole transition moment, the coupling efficiency to the individual modes can be controlled to a high degree. We finally showed that SiNWs can be used to filter single photons not only by their wavelength, but that it is furthermore possible to tailor the system such that single photons can be selected as function of the associated emitter orientation.

Our study demonstrates the high potential of crys-

talline silicon nanowires as functional and low loss nano-channels for quantum nano-photonics. Their rich modal landscape offers a tool for genuine modal engineering, enabling spectral sorting and emitter-orientation selection in the single photon regime. We emphasize that the SiNWs represent a totally un-optimized model system and we foresee that the here demonstrated single-photon modal engineering by high-index dielectric nanostructures can be strongly optimized using numerical design methods like evolutionary optimization or deep learning

based inverse design [45–48].

MATERIALS AND METHODS

Confocal and image plane luminescence acquisitions

The nanodiamonds coupled to Si nanowires have been studied by confocal and image plane luminescence microscopies. A linearly polarized cw excitation laser at λ_L=532 nm is focused on the sample with a x100 high numerical aperture air objective (NA=0.9). The luminescence is collected through a dichroic mirror (Semrock) centered at λ_L=550 nm. The sample is positioned on a xy piezoscanner. Once the excitation spot is parked on a specific location, the acquisition is performed either on a sensitive EMCCD camera (Andor Ixon 3) with a bandpass filter (Semrock - λ_c=692±40 nm) for the image plane snapshots, or through a 75-μm pinhole on a CCD camera (Andor Newton DU920P-BVF) coupled to spectrometer (Andor Shamrock 303i) with a 300-grooves-per-mm grating and a longpass filter (Thorlabs - λ_{lp}=600 nm). When excitation (in) and acquisition (out) need to be spatially separated on the sample, the pinhole can be moved off-axis in a conjugated xy image plane.

Silicon on Silica Substrate Fabrication and Electron Beam Lithography Structuration

To be able to perform confocal measurements in our inverted microscope in transmission configuration, we fabricated our samples on what we call "silicon-on-silica" (SOS) substrates. By thermal oxidation and subsequent oxide removal, we thin in a first step the silicon layer of commercial silicon-on-insulator (SOI) substrates until we reach the target thickness of 90 nm. Via wafer bonding we then combine the thinned SOI with a fused silica substrate. We note that the annealing during the bonding process is limited to temperatures around 200°C, due to the large mismatch in the thermal expansion coefficients of silicon and silica.[25] In order to obtain good adherence properties, we prepare the SOI surface in a nitrogen plasma. The surface of the fused silica substrate is treated in a chemical-mechanical preparation process. Finally, the silicon substrate and BOX (burried oxide) layer of the former SOI are removed from the bonded wafer via grinding and chemical etching, leaving only the 90 nm silicon layer on the fused silica substrate.

The structuration of these transparent SOS substrates is done in a top-down approach using electron beam lithography (EBL) and subsequent anisotropic plasma etching, in order to define rectangular Si nanowires (NWs) of different dimensions (the height is constant, defined by the thickness of the SOI silicon layer, which is 90 nm in our case. EBL is done on a $\approx$ 60 nm thick layer

of negative-tone resist (hydrogen silsesquioxane, "HSQ") with a RAITH 150 writer (electron energy of 30 keV). The resist is developed for 1 min in a solution of 25 % tetramethylammonium hydroxide (TMAH). The physical structuration of the silicon over-layer is finally done by reactive ion etching (RIE) in an SF_6/C_4F_8 plasma down to the silica substrate, following in-situ control.[23, 24]

We note that approximately 20 nm of developed resist (SiO_x with similar optical properties as SiO_2) remains on the nanowires. We did not observe any major impact of this top-layer on the optical properties, which we attribute to its small size and low refractive index. Removal of the residual layer with HF-etching resulted in destruction of the smallest nanowires due to under-etching, hence we decided to leave the SiO_x layer on all nanowires for better comparability.

SEM imaging was performed carefully with very low acceleration voltage, in order to limit electric charging of the isolating surface.

CONFLICT OF INTEREST

There are no conflicts to declare.

---

[1] Lan-Tian Feng, Guang-Can Guo, and Xi-Feng Ren. Progress on Integrated Quantum Photonic Sources with Silicon. Advanced Quantum Technologies, 3(2):1900058, 2020. ISSN 2511-9044. doi: 10.1002/qute.201900058.

[2] Peter Lodahl. Quantum-dot based photonic quantum networks. Quantum Science and Technology, 3(1): 013001, October 2017. ISSN 2058-9565. doi: 10.1088/2058-9565/aa91bb.

[3] A. Femius Koenderink. Single-photon nanoantennas. ACS Photonics, 4(4):710–722, 2017.

[4] Jianwei Wang, Fabio Sciarrino, Anthony Laing, and Mark G. Thompson. Integrated photonic quantum technologies. Nature Photonics, 14(5):273–284, May 2020. ISSN 1749-4893. doi: 10.1038/s41566-019-0532-1.

[5] R. E. Evans, M. K. Bhaskar, D. D. Sukachev, C. T. Nguyen, A. Sipahigil, M. J. Burek, B. Machielse, G. H. Zhang, A. S. Zibrov, E. Bielejec, H. Park, M. Loncar,

and M. D. Lukin. Photon-mediated interactions between quantum emitters in a diamond nanocavity. Science, 362 (6415):662–665, November 2018. ISSN 0036-8075, 1095-9203. doi: 10.1126/science.aau4691.

[6] A. V. Akimov, A. Mukherjee, C. L. Yu, D. E. Chang, A. S. Zibrov, P. R. Hemmer, H. Park, and M. D. Lukin. Generation of single optical plasmons in metallic nanowires coupled to quantum dots. Nature, 450 (7168):402–406, November 2007. ISSN 1476-4687. doi: 10.1038/nature06230.

[7] Alexander Huck, Shailesh Kumar, Abdul Shakoor, and Ulrik L. Andersen. Controlled Coupling of a Single Nitrogen-Vacancy Center to a Silver Nanowire. Physical Review Letters, 106(9):096801, February 2011. doi: 10.1103/PhysRevLett.106.096801.

[8] Esteban Bermúdez-Ureña, Carlos Gonzalez-Ballestero, Michael Geiselmann, Renaud Marty, Ilya P. Radko, Tobias Holmgaard, Yury Alaverdyan, Esteban Moreno, Francisco J. García-Vidal, Sergey I. Bozhevolnyi, and Romain Quidant. Coupling of individual quantum emitters to channel plasmons. Nature Communications, 6 (1):7883, August 2015. ISSN 2041-1723. doi: 10.1038/ncomms8883.

[9] Christian Schörner, Subhasis Adhikari, and Markus Lippitz. A Single-Crystalline Silver Plasmonic Circuit for Visible Quantum Emitters. Nano Letters, 19(5):3238–3243, May 2019. ISSN 1530-6984. doi: 10.1021/acs.nanolett.9b00773.

[10] Shailesh Kumar, Sebastian K. H. Andersen, and Sergey I. Bozhevolnyi. Extremely Confined Gap-Plasmon Waveguide Modes Excited by Nitrogen-Vacancy Centers in Diamonds. ACS Photonics, 6(1):23–29, January 2019. doi: 10.1021/acsphotonics.8b01225.

[11] Mikhail Y. Shalaginov, Simeon I. Bogdanov, Alexei S. Lagutchev, Alexander V. Kildishev, Alexandra Boltasseva, and Vladimir M. Shalaev. On-Chip Single-Layer Integration of Diamond Spins with Microwave and Plasmonic Channels. ACS Photonics, 7(8):2018–2026, August 2020. doi: 10.1021/acsphotonics.0c00325.

[12] Roman Kolesov, Bernhard Grotz, Gopalakrishnan Balasubramanian, Rainer J. Stöhr, Aurélien A. L. Nicolet, Philip R. Hemmer, Fedor Jelezko, and Jörg Wrachtrup. Wave–particle duality of single surface plasmon polaritons. Nature Physics, 5(7):470–474, July 2009. ISSN 1745-2481. doi: 10.1038/nphys1278.

[13] Aurélien Cuche, Oriane Mollet, Aurélien Drezet, and Serge Huant. "Deterministic" Quantum Plasmonics. Nano Letters, 10(11):4566–4570, November 2010. ISSN 1530-6984. doi: 10.1021/nl102568m.

[14] M. S. Tame, K. R. McEnery, Ş K. Özdemir, J. Lee, S. A. Maier, and M. S. Kim. Quantum plasmonics. Nature Physics, 9(6):329, June 2013. ISSN 1745-2481. doi: 10.1038/nphys2615.

[15] Günter Kewes, Max Schoengen, Oliver Neitzke, Pietro Lombardi, Rolf-Simon Schönfeld, Giacomo Mazzamuto, Andreas W. Schell, Jürgen Probst, Janik Wolters, Bernd Löchel, Costanza Toninelli, and Oliver Benson. A realistic fabrication and design concept for quantum gates based on single emitters integrated in plasmonic-dielectric waveguide structures. Scientific Reports, 6 (1):28877, July 2016. ISSN 2045-2322. doi: 10.1038/srep28877.

[16] Hamidreza Siampour, Shailesh Kumar, and Sergey I. Bozhevolnyi. Chip-integrated plasmonic cavity-enhanced single nitrogen-vacancy center emission. Nanoscale, 9 (45):17902–17908, November 2017. ISSN 2040-3372. doi: 10.1039/C7NR05675C.

[17] Jean-Claude Weeber, Kamal Hammani, Gerard Colas-des-Francs, Alexandre Bouhelier, Juan Arocas, Arunandan Kumar, Fabien Eloi, Stéphanie Buil, Xavier Quélin, Jean-Pierre Hermier, Michel Nasilowski, and Benoit Dubertret. Colloidal Quantum Dot Integrated Light Sources for Plasmon Mediated Photonic Waveguide Excitation. ACS Photonics, 3(5):844–852, May 2016. doi: 10.1021/acsphotonics.6b00054.

[18] Shailesh Kumar and Sergey I. Bozhevolnyi. Excitation of Hybrid Plasmonic Waveguide Modes by Colloidal Quantum Dots. ACS Photonics, 6(7):1587–1593, July 2019. doi: 10.1021/acsphotonics.9b00379.

[19] Pavel Kolchin, Nitipat Pholchai, Maiken H. Mikkelsen, Jinyong Oh, Sadao Ota, M. Saif Islam, Xiaobo Yin, and Xiang Zhang. High Purcell Factor Due To Coupling of a Single Emitter to a Dielectric Slot Waveguide. Nano Letters, 15(1):464–468, January 2015. ISSN 1530-6984. doi: 10.1021/nl5037808.

[20] Pablo Albella, M. Ameen Poyli, Mikolaj K. Schmidt, Stefan A. Maier, Fernando Moreno, Juan José Sáenz, and Javier Aizpurua. Low-Loss Electric and Magnetic Field-Enhanced Spectroscopy with Subwavelength Silicon Dimers. The Journal of Physical Chemistry C, 117(26):13573–13584, July 2013. ISSN 1932-7447. doi: 10.1021/jp4027018.

[21] Michela F. Picardi, Anatoly V. Zayats, and Francisco J. Rodríguez-Fortuño. Amplitude and Phase Control of Guided Modes Excitation from a Single Dipole Source: Engineering Far- and Near-Field Directionality. Laser & Photonics Reviews, 13(12):1900250, 2019. ISSN 1863-8899. doi: 10.1002/lpor.201900250.

[22] Alison E. Rugar, Constantin Dory, Shahriar Aghaeimeibodi, Haiyu Lu, Shuo Sun, Sattwik Deb Mishra, Zhi-Xun Shen, Nicholas A. Melosh, and Jelena Vucković. Narrow-

Linewidth Tin-Vacancy Centers in a Diamond Waveguide. ACS Photonics, 7(9):2356–2361, September 2020. doi: 10.1021/acsphotonics.0c00833.

[23] Xiang-Lei Han, Guilhem Larrieu, Pier-Francesco Fazzini, and Emmanuel Dubois. Realization of ultra dense arrays of vertical silicon nanowires with defect free surface and perfect anisotropy using a top-down approach. Microelectronic Engineering, 88(8):2622–2624, August 2011. ISSN 0167-9317. doi: 10.1016/j.mee.2010.12.102.

[24] Y. Guerfi, F. Carcenac, and G. Larrieu. High resolution HSQ nanopillar arrays with low energy electron beam lithography. Microelectronic Engineering, 110:173–176, October 2013. ISSN 0167-9317. doi: 10.1016/j.mee.2013.03.055.

[25] H. Moriceau, F. Fournel, and F. Rieutord. Materials and manufacturing techniques for SOI wafer technology. In O. Kononchuk and B.-Y. Nguyen, editors, Silicon-on-Insulator (SOI) Technology, pages 38–46. Woodhead Publishing, 2014. ISBN 978-0-85709-925-9.

[26] Arseniy I. Kuznetsov, Andrey E. Miroshnichenko,

Yuan Hsing Fu, JingBo Zhang, and Boris Luk'yanchuk. Magnetic light. Scientific Reports, 2:492, July 2012. ISSN 2045-2322. doi: 10.1038/srep00492.

[27] Peter R. Wiecha, Clément Majorel, Christian Girard, Arnaud Arbouet, Bruno Masenelli, Olivier Boisron, Aurélie Lecestre, Guilhem Larrieu, Vincent Paillard, and Aurélien Cuche. Enhancement of electric and magnetic dipole transition of rare-earth-doped thin films tailored by high-index dielectric nanostructures. Applied Optics, 58(7):1682–1690, March 2019. ISSN 2155-3165. doi: 10.1364/AO.58.001682.

[28] Davy Gérard, Jérôme Wenger, Alexis Devilez, David Gachet, Brian Stout, Nicolas Bonod, Evgeny Popov, and Hervé Rigneault. Strong electromagnetic confinement near dielectric microspheres to enhance single-molecule fluorescence. Optics Express, 16(19):15297–15303, September 2008. ISSN 1094-4087. doi: 10.1364/OE.16.015297.

[29] Houssem Kallel, Arnaud Arbouet, Marzia Carrada, Gérard Ben Assayag, Abdallah Chehaidar, Priyanka Periwal, Thierry Baron, Pascal Normand, and Vincent Paillard. Photoluminescence enhancement of silicon nanocrystals placed in the near field of a silicon nanowire. Physical Review B, 88(8):081302, August 2013. doi: 10.1103/PhysRevB.88.081302.

[30] Yuan Hsing Fu, Arseniy I. Kuznetsov, Andrey E. Miroshnichenko, Ye Feng Yu, and Boris Luk'yanchuk. Directional visible light scattering by silicon nanoparticles. Nature Communications, 4:1527, February 2013. doi: 10.1038/ncomms2538.

[31] Peter R. Wiecha, Aurélien Cuche, Arnaud Arbouet, Christian Girard, Gérard Colas des Francs, Aurélie Lecestre, Guilhem Larrieu, Frank Fournel, Vincent Larrey, Thierry Baron, and Vincent Paillard. Strongly Directional Scattering from Dielectric Nanowires. ACS Photonics, 4(8):2036–2046, August 2017. doi: 10.1021/acsphotonics.7b00423.

[32] A. Cuche, M. Berthel, U. Kumar, G. Colas des Francs, S. Huant, E. Dujardin, C. Girard, and A. Drezet. Near-field hyperspectral quantum probing of multimodal plasmonic resonators. Physical Review B, 95(12):121402, March 2017. doi: 10.1103/PhysRevB.95.121402.

[33] S. V. Makarov, I. S. Sinev, V. A. Milichko, F. E. Komissarenko, D. A. Zuev, E. V. Ushakova, I. S. Mukhin, Y. F. Yu, A. I. Kuznetsov, P. A. Belov, I. V. Iorsh, A. N. Poddubny, A. K. Samusev, and Yu. S. Kivshar. Nanoscale Generation of White Light for Ultrabroadband Nanospectroscopy. Nano Letters, 18(1):535–539, January 2018. ISSN 1530-6984. doi: 10.1021/acs.nanolett.7b04542.

[34] Upkar Kumar, Sreenath Bolisetty, Raffaele Mezzenga, Christian Girard, Erik Dujardin, and Aurélien Cuche. Single plasmon spatial and spectral sorting on a crystalline two-dimensional plasmonic platform. Nanoscale, 12(25):13414–13420, July 2020. ISSN 2040-3372. doi: 10.1039/D0NR02066D.

[35] Christian Girard. Near fields in nanostructures. Reports on Progress in Physics, 68(8):1883–1933, August 2005. ISSN 0034-4885, 1361-6633. doi: 10.1088/0034-4885/68/8/R05.

[36] Olivier J. F. Martin, Christian Girard, and Alain Dereux. Generalized Field Propagator for Electromagnetic Scattering and Light Confinement. Physical Review Letters, 74(4):526–529, January 1995. doi: 10.1103/PhysRevLett.74.526.

[37] Peter R. Wiecha. pyGDM—A python toolkit for full-field electro-dynamical simulations and evolutionary optimization of nanostructures. Computer Physics Communications, 233:167–192, December 2018. ISSN 0010-4655. doi: 10.1016/j.cpc.2018.06.017.

[38] David F. Edwards. Silicon (Si)*. In Edward D. Palik, editor, Handbook of Optical Constants of Solids, pages 547–569. Academic Press, Burlington, 1997. ISBN 978-0-12-544415-6.

[39] Clément Majorel, Christian Girard, Aurélien Cuche, Arnaud Arbouet, and Peter R. Wiecha. Quantum theory of near-field optical imaging with rare-earth atomic clusters. JOSA B, 37(5):1474–1484, May 2020. ISSN 1520-8540. doi: 10.1364/JOSAB.385918.

[40] J. Barthes, G. Colas des Francs, A. Bouhelier, J.-C. Weeber, and A. Dereux. Purcell factor for a point-like dipolar emitter coupled to a two-dimensional plasmonic waveguide. Physical Review B, 84(7):073403, August 2011. doi: 10.1103/PhysRevB.84.073403.

[41] Gérard Colas des Francs, Jonathan Grandidier, Sébastien Massenot, Alexandre Bouhelier, Jean-Claude Weeber, and Alain Dereux. Integrated plasmonic waveguides: A mode solver based on density of states formulation. Physical Review B, 80(11):115419, September 2009. doi: 10.1103/PhysRevB.80.115419.

[42] Olivier J. F. Martin and Nicolas B. Piller. Electromagnetic scattering in polarizable backgrounds. Physical Review E, 58(3):3909–3915, September 1998. doi: 10.1103/PhysRevE.58.3909.

[43] G. Colas des Francs, J. Barthes, A. Bouhelier, J. C. Weeber, A. Dereux, A. Cuche, and C. Girard. Plasmonic Purcell factor and coupling efficiency to surface plasmons. Implications for addressing and controlling optical nanosources. Journal of Optics, 18(9):094005, August 2016. ISSN 2040-8986. doi: 10.1088/2040-8978/18/9/094005.

[44] Christian Laube, Thomas Oeckinghaus, Jan Lehnert, Jan Griebel, Wolfgang Knolle, Andrej Denisenko, Axel Kahnt, Jan Meijer, Jörg Wrachtrup, and Bernd Abel. Controlling the fluorescence properties of nitrogen vacancy centers in nanodiamonds. Nanoscale, 11(4):1770–1783, January 2019. ISSN 2040-3372. doi: 10.1039/C8NR07828A.

[45] Peter R. Wiecha, Arnaud Arbouet, Christian Girard, Aurélie Lecestre, Guilhem Larrieu, and Vincent Paillard. Evolutionary multi-objective optimization of colour pixels based on dielectric nanoantennas. Nature Nanotechnology, 12(2):163–169, February 2017. ISSN 1748-3387. doi: 10.1038/nnano.2016.224.

[46] Nicholas J. Dinsdale, Peter R. Wiecha, Matthew Delaney, Jamie Reynolds, Martin Ebert, Ioannis Zeimpekis, David J. Thomson, Graham T. Reed, Philippe Lalanne, Kevin Vynck, and Otto L. Muskens. Deep learning enabled design of complex transmission matrices for universal optical components. ACS Photonics, ASAP, 2021. doi: 10.1021/acsphotonics.0c01481.

[47] Peter R. Wiecha, Peter R. Wiecha, Clément Majorel, Christian Girard, Aurélien Cuche, Vincent Paillard, Otto L. Muskens, and Arnaud Arbouet. Design of plasmonic directional antennas via evolutionary optimization. Optics Express, 27(20):29069–29081, September 2019. ISSN 1094-4087. doi: 10.1364/OE.27.029069.

[48] Logan Su, Alexander Y. Piggott, Neil V. Sapra, Jan

Petykiewicz, and Jelena Vucković. Inverse Design and Demonstration of a Compact on-Chip Narrowband Three-Channel Wavelength Demultiplexer. ACS Photonics, 5(2):301–305, February 2018. doi: 10.1021/acsphotonics.7b00987.